



Research Article

Environmentally sustainable facile synthesis of nanocrystalline holmium hafnate ($\text{Ho}_2\text{Hf}_2\text{O}_7$): Promising new oxide-ion conducting solid electrolyte

Suneela Sardar¹ · Girish Kale¹  · Oscar Cespedes² · Mojtaba Ghadiri¹

Received: 7 October 2019 / Accepted: 25 February 2020 / Published online: 3 March 2020
© The Author(s) 2020 

Abstract

$\text{A}_2\text{B}_2\text{O}_7$ oxides with defect-fluorite structure are one of the potential candidates for solid oxide fuel cell electrolyte material due to their excessive thermodynamic stability in oxygen potential gradient at elevated temperature between 500 and 900 °C. Holmium hafnate nanoparticles have been synthesised through the Leeds Alginate Process (LAP) using inorganic salts of holmium and hafnium as starting materials immobilized in alginate beads. Ion exchange with sodium alginate and its subsequent thermal treatment have been used to prepare the nanopowder of $\text{Ho}_2\text{Hf}_2\text{O}_7$. Thermal decomposition of dried beads is carried out at 700 °C for 2 h and 6 h to obtain the nanoparticles of $\text{Ho}_2\text{Hf}_2\text{O}_7$. This calcination temperature was determined after carrying out simultaneous thermogravimetric analysis and differential scanning calorimetry (TGA/DSC). High Temperature X-ray Diffraction (HT-XRD) was carried out to gain further insight into the thermal decomposition process in static ambient environment. HT-XRD analysis corroborated with the results obtained from TGA/DSC. Nanocrystalline powder of single phase $\text{Ho}_2\text{Hf}_2\text{O}_7$ has been obtained by calcination of oven dried ion-exchanged alginate beads in relatively low temperature range of 500–700 °C. Rietveld refinement of X-ray diffraction (XRD) data confirmed the formation of single phase defect fluorite structure of $\text{Ho}_2\text{Hf}_2\text{O}_7$. The crystallographic parameters calculated from TEM and XRD analysis are in excellent agreement with each other. Furthermore, TEM–EDX analysis confirms that the $\text{Ho}_2\text{Hf}_2\text{O}_7$ synthesised by the facile alginate process is nearly stoichiometric. Raman spectroscopy gives evidence of the presence of oxide-ion vacancy in holmium hafnate which is supported with ac-impedance spectroscopy measurement at selected three temperatures. The present study suggests that the LAP has the capability of yielding on a large scale single phase defect-fluorite nanoparticles of electrolyte materials for solid oxide fuel cells in environmentally sustainable, economical and energy efficiently manner.

Keywords Alginate synthesis · Nanoparticles · Holmium hafnate · Fluorite · Electrolytes · Fuel cells

1 Introduction

Solid Oxide Fuel Cells (SOFCs) are an efficient and cost effective system for direct conversion of a variety of fuels to electricity [1]. High temperature operation of SOFC may cause problem of accelerating corrosion, degeneration and instability of components. To overcome this issue specialized materials for different parts of cell are required

[2]. Electrolyte having high ionic conductivity with transport number of ions close to unity and a transport number of electrons close to zero is significant in lowering the operating temperature and maintaining high conversion efficiency of SOFC [3].

Ternary oxides having general formula of $\text{A}_2\text{B}_2\text{O}_7$ depict crystal structure of pyrochlore or fluorite type. Pyrochlore is derived from fluorite by removing oxygen anion at 8a

✉ Girish Kale, g.m.kale@leeds.ac.uk | ¹School of Chemical and Process Engineering, University of Leeds, Leeds LS2 9JT, UK. ²School of Physics and Astronomy, University of Leeds, Leeds LS2 9JT, UK.



site and ordering in cation sub-lattice. Consequently, ordered pyrochlore ($Fd\bar{3}m$) can be differentiated from fluorite ($Fm\bar{3}m$) by the superlattice coming from ordering both in anionic and cationic sublattice. Larger trivalent rare earth elements with eightfold co-ordinated cations occupy A-site. Smaller and tetravalent transition metals with 6-fold co-ordinated cations like Zr, Ti and Hf occupy site-B [4]. Pyrochlore structured composition have a wide range of technically important properties such as high ionic conductivity, superconductivity, luminescence and ferromagnetism [5]. Lanthanide based pyrochlore are emerging as an important class of solid oxide materials with potential applications as ionic conductors [6], thermal barrier coatings [7], nuclear waste storage materials [8], scintillators and semiconductors [9]. These applications are due to the structural flexibility of pyrochlores and specifically mobility of anions [10].

Morphology and microstructure of cell components are very important for durability and performance of SOFC. Sol gel processes are used to fabricate the electrolyte and electrode materials of SOFC with preferred properties or functionalities, as they are capable of providing good control of crystal structure, composition, microstructure and morphology [11]. Nanopowders of CGO (Cerium Gadolinium Oxide) and NiO have been successfully prepared by Leeds Alginate Process (LAP) for electrolyte and anode applications in a SOFC which is a unique polysaccharide mediated ion-exchange process developed by Kale et al. [12, 13].

$\text{Ho}_2\text{Hf}_2\text{O}_7$ has been prepared mechanochemically [14, 15] and thermodynamically [16] for metal-oxide semiconductor devices [15], electrochemical devices [15] and nuclear waste storage materials [8]. Mechanochemical synthesis of holmium hafnate involved the extensive ball milling and overnight heating at 900 °C [14] and in other case ball milling of holmium and hafnium salts followed by calcination at 1500 °C for 24 h [15]. Synthesis of holmium

hafnate thermodynamically involved the three heating protocol of 1200 °C for 36 h, 1300 °C for 36 h and 1400 °C for 48 h along with intermittent grinding [16]. However, it is important to prepare this material in an environment-friendly and cost effective manner as the previously used methods involve extensive milling and repetitive high temperature heating protocol, respectively.

Sodium alginate is a large molecular weight polysaccharide with general formula $(\text{C}_6\text{H}_7\text{NaO}_6)_n$ and is extracted from brown seaweeds. It has varying amounts of α -L-guluronic acid (G) and 1,4 linked β -D-mannuronic acid (M) residues linked together covalently in different sequence such as –MM– or –GG– structures or –GM– block copolymers as shown in Fig. 1. In aqueous solution, multivalent metal ions (Ho^{3+} and Hf^{4+}) interact with the carboxylic group of alginate forming 'egg-box' like structures. Metal ions generally prefer to bind on G blocks of alginate molecules during the ion-exchange process [17]. Metal ions immobilize during gelation and drying processes whereas they convert to metal oxides on calcination in ambient atmosphere. As the alginate structure collapse during the calcination, limited proximity of metal oxides suppresses agglomeration and grain growth thus leading to the formation of crystalline nanoparticles [18, 19].

In this research article we describe a successful application of LAP for the first time for the facile synthesis of high purity single phase nanocrystalline powder of $\text{Ho}_2\text{Hf}_2\text{O}_7$ after thermal decomposition of oven dried ion-exchanged metal alginate beads. In order to understand the thermal decomposition process of ion-exchanged metal alginate beads, the product was characterised using simultaneous thermogravimetric analysis and differential scanning calorimetry (TGA/DSC) and High Temperature X-ray Diffraction (HT-XRD). Structural and morphological characterisation of the nanoparticles was carried out using X-ray diffraction (XRD) coupled with size/strain Rietveld refinement, Raman spectroscopy and Transmission Electron

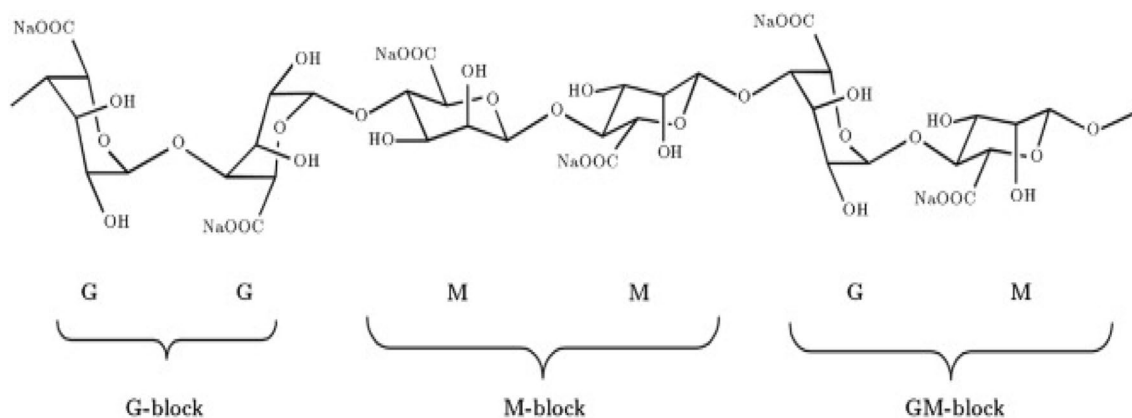


Fig. 1 Structure of Na-Alginate in chain conformation [19]

Microscopy (TEM) combined with Energy Dispersive X-ray (EDX) spectroscopy.

2 Experimental detail

2.1 Materials

Commercially available holmium (III) nitrate pentahydrate, $\text{Ho}(\text{NO}_3)_3 \cdot 5\text{H}_2\text{O}$ (purity 99.9%) and hafnium (IV) tetrachloride, HfCl_4 (purity 99.9%) were purchased from Alfa Aesar (Heysham, UK). Sodium alginate (Na-ALG) was purchased from Sigma Aldrich Company Ltd. (Birmingham, UK).

2.2 Synthesis of metal-alginate beads

Solution of sodium alginate with the concentration of 4 wt% was prepared by dissolving appropriate quantity of sodium alginate in distilled water under magnetic stirring. Metal complex solution was prepared by dissolving respective quantities of metal salts to obtain molar ratio of $\text{Ho}^{3+}/\text{Hf}^{4+} = 1$ in distilled water using magnetic stirrer. Both the ionic solutions were prepared at an ambient temperature and pressure. Metal alginate beads were prepared by dripping 200 ml of sodium alginate solution from a burette into 200 ml of metal complex solution contained in a pyrex glass beaker. The beads were about 4 mm in diameter and

have a small tail as the fall height was inadequate for the drops to come to a spherical shape before coming in contact with the metal ion solution. Larger fall heights would give nearly spherical beads. Beads were maintained in aqueous metal ion solution overnight with gentle magnetic stirring to allow complete ion exchange of Na^+ with Ho^{3+} and Hf^{4+} . Beads were then separated from the solution by straining through a stainless steel sieve. Metal alginate beads were washed with distilled water several time to remove any unreacted material. Drying of beads was carried out in convection oven at 90°C for 24 h producing fully dry beads. The morphology of wet and dried beads is shown in Fig. 2.

2.3 Characterisation

Thermal analysis of dried beads was carried out employing a Mettler Toledo STAR[®] System (Leicester, UK) which simultaneously performed Thermogravimetric Analysis (TGA) and Differential Scanning Calorimetry (DSC) investigations. The TGA and DSC experiments were performed in a controlled atmosphere of flowing air at the rate of 10 mL min^{-1} . Simultaneous TGA/DSC analyses were carried out from room temperature to 900°C at the heating rate of $10^\circ\text{C min}^{-1}$ without any holding time. Initial sample mass used in this analysis was adjusted at about 19 mg.

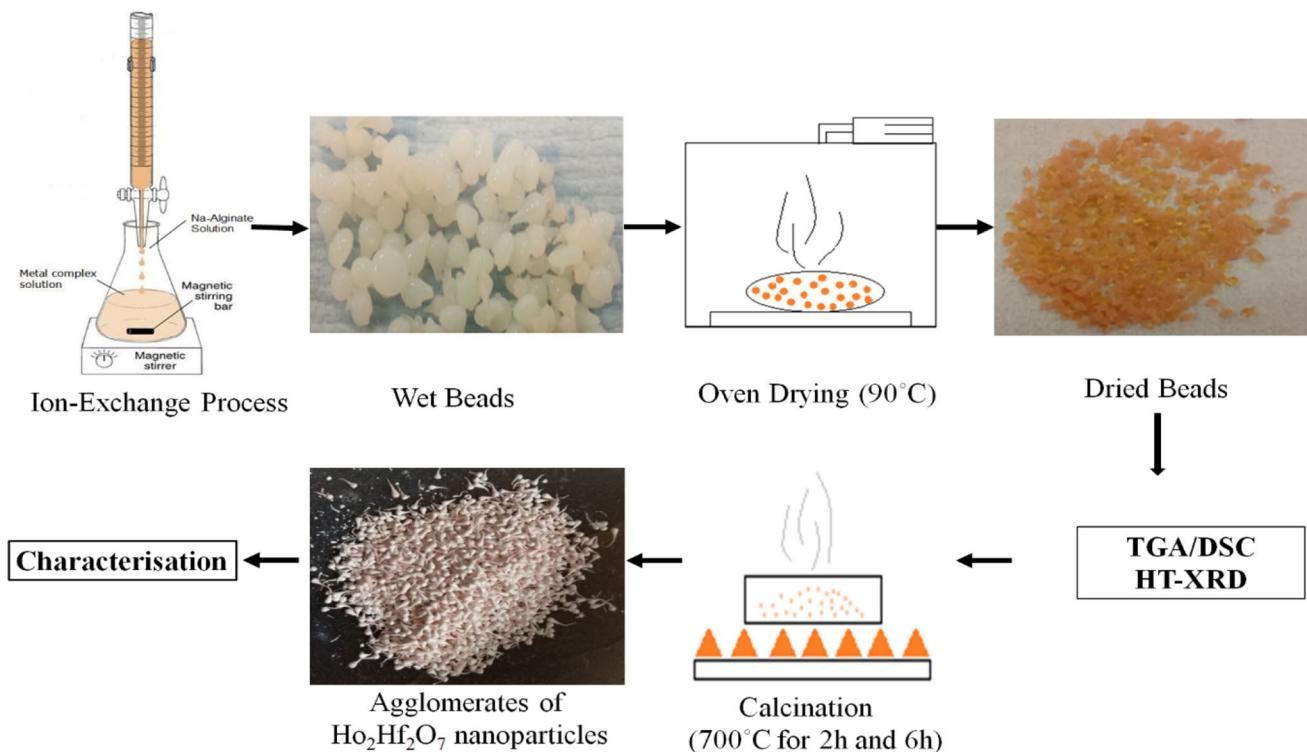


Fig. 2 Schematic flow diagram for the synthesis of $\text{Ho}_2\text{Hf}_2\text{O}_7$ nanopowders employing LAP

The dried metal alginate beads were milled to reduce diffusion time by employing Retsch Shaker Mill at the frequency of 30 Hz using steel ball to obtain fine powder for High Temperature X-ray diffraction (HT-XRD) analysis, employing CuK α radiation ($\lambda = 1.5418 \text{ \AA}$) (Anton Paar HTK-1200, Almelo, The Netherlands) at 40 kV and 40 mA. The temperature program was set to increase the sample temperature from room temperature to 1000 °C with the interval of 25 °C at the heating rate of 10 °C min⁻¹ in static air condition. Dwell time of 30 min was provided at each temperature to allow the attainment of complete thermal equilibration of the sample. Scan for HT-XRD was performed over a 2 θ ranges from 20° to 80° with the step size of 0.03°. To obtain the information of phases present a total scan time of 20 min was provided. This system employs the X'cellerator multi-detector which causes surd (irrational) in step size. Programmable divergence and antiscatter slits were used for generating constant irradiation length on the sample to improve the data collection statistics at higher angles and reducing the effect of air scattering at low angles which has been known to influence the background of X-ray diffraction patterns. The data were converted from automatic to fixed slit to make it suitable for structural analysis. Resultant data were analysed using software package X'Pert High Score plus (P'Analytical, The Netherlands).

In a separate instance the nanopowder of Ho₂Hf₂O₇ was analysed using powder X-ray diffraction (XRD Bruker D8) employing CuK α radiation ($\lambda = 1.5418 \text{ \AA}$) at ambient conditions. A Rietveld size/strain structural refinement was performed on the data obtained from XRD. P'Analytical X'Pert High Score plus software package was used for Rietveld refinement, detail of which can be found elsewhere [19–22]. Data comprised of Gaussian and Lorentzian components and a Pseudo-Voigt profile was used to refine the relative proportion of each component during the refinement process.

Raman spectroscopy was used to study the local structure of the prepared nanoparticles. Raman spectra was collected using a Horiba Raman system with three different excitation laser wavelength of 473 nm, 514 nm and 633 nm at an excitation intensity of 25 mW and data acquisition time of 10 s. The Raman band of silicon wafer at $520.5 \pm 0.5 \text{ cm}^{-1}$ was used to calibrate the spectrometer. Raman spectra was collected and analysed using Origin Pro software.

Finally, holmium hafnate nanopowders were inspected using Transmission Electron Microscopy (FEI Tecnai TF20 FEG-TEM, Eindhoven, The Netherlands) for particle size, crystallinity, interplanar spacing and morphological features. Energy Dispersive X-ray (EDX) spectroscopy was used to estimate the elemental composition. Preliminary measurements of ac-impedance spectroscopy were

carried out on the high density sintered pellet of holmium hafnate at three different temperature i.e. 400 °C, 600 °C and 750 °C over the frequency range of 100 mHz to 100 MHz in order to determine the oxide-ion conductivity of the material. Figure 2 shows the schematic process flow diagram of LAP for the synthesis of nanoparticles of Ho₂Hf₂O₇.

3 Results and discussions

Thermal analysis of dried beads was carried out using TGA/DSC and the result of the analysis is shown in Fig. 3 along with Differential Thermogravimetry (DTG) trace. Thermal decomposition of dried beads involved six stages of phase transformation. These six thermal decomposition stages were identified to be ranging from 40–120 °C, 150–210 °C, 217–375 °C, 375–485 °C, 485–535 °C and 535–565 °C, respectively. In TGA/DTG profile decomposition steps agreed well with DSC curve as shown in Fig. 3. In DSC profile two small endothermic peaks were observed in the range 41–108 °C and 160–178 °C which is due to the loss of water during heat treatment. In TGA curve weight losses of 10% was observed in the first stage due to the removal of adsorbed water. Evaporation of bounded water and dissociation of alginate structure (GG–O–MM, MM–O–GM) along with evolution of bridging oxygen [13] were observed in the range 150–210 °C with corresponding weight loss of 17%. A weight loss of 23% was observed in the range 217–375 °C due to further loss of bridging oxygen and partially reacting with some of carbon atoms in the chain to form CO₂. In DSC profile an exothermic band was observed from 205–365 °C due to this partial reaction and splitting of weaker linkages (G–G, G–M and M–M) in the alginate polysaccharide molecule [13]. Two exothermic peaks were observed in DSC profile in the ranges 372–485 °C and 485–573 °C. These

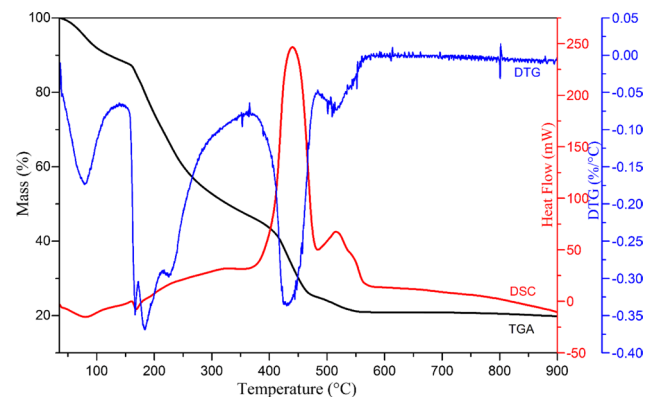


Fig. 3 TGA/DSC/DTG analysis of dry beads

peaks were the result of oxidative decomposition of metal-alginate beads. Weight loss of 21% was observed from 375 to 485 °C due to the bulk oxidation of alginate to form CO₂. Complete decomposition of β-D-mannuronic acid (M) and α-L-guluronic acid (G) residues [13] was observed with weight loss of 3% and formation of binary metal oxides in the range 485–535 °C. In the DSC curve a shoulder in second exothermic peak was observed at 535 °C. Formation of tertiary oxides was observed in the range 535–565 °C with minor weight loss of 1%. Based on TGA/DTG/DSC analysis the calcination temperature of 700 °C was determined to be the safe optimum temperature for the formation of phase pure Ho₂Hf₂O₇ which is the lowest temperature reported in literature for the formation of this compound.

HT-XRD was performed on milled beads from room temperature to 1000 °C at the rate of 10 °C min⁻¹ in stationary air on α-Al₂O₃ sample holder.

Figure 4 shows the HT-XRD patterns of oven dried metal alginate beads after eliminating α-Al₂O₃ peaks by refining the observed data. At temperature 400–500 °C peaks of holmium hafnate started appearing along with sample holder peaks. Clearly a single phase cubic defect-fluorite Ho₂Hf₂O₇ pattern appeared to have evolved from alginate matrix at 500 °C. At 600 °C, single phase holmium hafnate pattern with high purity was clearly seen after complete

thermal decomposition followed by crystallisation of metal-alginate beads which is in good agreement with transformation temperature observed in TGA/DSC analysis. It is apparent that the onset of decomposition occurred at 400 °C and ended at 600 °C with the formation of high purity nanoparticles of Ho₂Hf₂O₇. Further increase in temperature from 700 to 1000 °C results in the XRD peaks becoming narrower, sharper and more intense due to the growth in crystal size [13].

Inset of Fig. 4 shows observed HT-XRD patterns of dried metal-alginate beads at selected temperatures of 100 °C, 700 °C and 1000 °C. α-Al₂O₃ peaks were observed throughout the scan from 25 to 1000 °C as some of the X-rays penetrated through metal alginate sample to the surface of sample holder. Apart from α-Al₂O₃ sample holder peaks, no peaks of any other unexpected material were observed above 400 °C which confirms the formation of high purity Ho₂Hf₂O₇ employing the alginate synthesis method (LAP) shown in Fig. 2.

Results of TGA/DSC and HT-XRD are in good agreement with each other showing complete thermal decomposition of dried metal alginate beads leading to the formation of nanocrystalline Ho₂Hf₂O₇ at 600 °C. Based on the Hess's law of heat summation it can be concluded from the results of TGA/DTG/DSC traces shown in Fig. 3 and HT-XRD

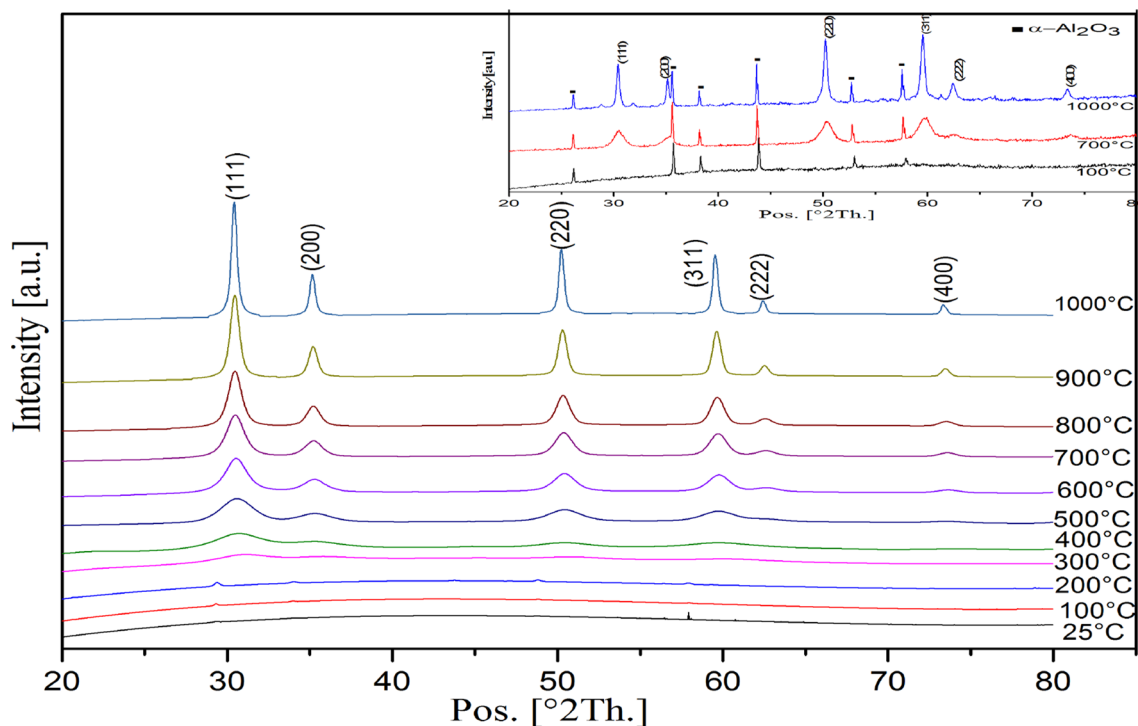


Fig. 4 HT-XRD patterns of metal alginate beads from 25 to 1000 °C, sample holder (α-Al₂O₃) peaks were digitally eliminated for clarity. The patterns are indexed by ICDD, 00-024-0473 with miller indices of crystal planes of cubic Ho₂Hf₂O₇ shown at the top of the peaks.

Inset shows the HT-XRD of dried metal-alginate beads at 100 °C, 700 °C and 1000 °C. Inset also shows the positions 'filled squares' of α-Al₂O₃ peaks from sample holder

patterns shown in Fig. 4 that the enthalpy change for the thermal decomposition of metal-alginate ($\text{Ho}^{3+}/\text{Hf}^{4+}$ —ALG) into $\text{Ho}_2\text{Hf}_2\text{O}_7$, $\text{CO}_{2(g)}$ and $\text{H}_2\text{O}_{(g)}$ is -6834 ± 683 J/g.

The net enthalpy change is calculated from the algebraic sum of the area under each peak in the DSC trace divided by the change in weight of the corresponding peak in TGA trace. The net enthalpy change of -6834 J/g ($\pm 10\%$) shows that over all decomposition process is exothermic in nature. It can be envisaged that in a continuous manufacturing process the evolved heat can be utilized for the drying and calcination process of beads or stored if it is produced in excess of the requirements thereby making the process either fully or partially self-sustainable.

Nanopowders of $\text{Ho}_2\text{Hf}_2\text{O}_7$ for further characterisation were obtained from dried beads calcined at 700°C for 2 h and 6 h in stationary air. During calcination the rate of $10^\circ\text{C min}^{-1}$ was maintained for both heating and cooling cycles. Thermal decomposition of the precursor formed the weakly-bonded agglomerates of $\text{Ho}_2\text{Hf}_2\text{O}_7$ nanoparticles which were converted into fine particles using mortar and pestle.

XRD analysis was performed of the nanopowders of $\text{Ho}_2\text{Hf}_2\text{O}_7$ after calcining at 700°C for 2 h and 6 h respectively. The observed data for different annealing time corresponded with the single phase cubic defect fluorite

structure of $\text{Ho}_2\text{Hf}_2\text{O}_7$ as shown in Fig. 5. The broadening of the peak is mainly due to the nano-sized crystallites, which is the characteristic of the materials synthesized by Leeds Alginate Process (LAP) [12]. Furthermore, as the calcination duration increases from 2 to 6 h coarsening takes place due to thermally assisted enhanced mass transport within the nanocrystals resulting into sharper and narrower XRD peaks.

Table 1 below shows the effect of calcination duration on crystallite size. Growth in crystallite size is because of Ostwald ripening in which crystal size increases with time at elevated temperature due to enhanced cationic ionic diffusion as large crystals are formed at the expense of smaller crystals. For longer calcination duration grain growth results in stable structure. The process will continue resulting in the growth of larger particles and correspondingly disappearance of smaller particles [13, 23].

Rietveld refinement of the XRD pattern of holmium hafnate ($\text{Ho}_2\text{Hf}_2\text{O}_7$) calcined at 700°C for 6 h is shown in Fig. 6. The observed and calculated patterns matched with each other and peaks are also indexed with the XRD reference pattern (ICDD, 00-024-0473). The observed and calculated patterns are in excellent agreement with each other as seen from the value of goodness of fit (GOF) close to unity in Table 1.

Fig. 5 XRD patterns of $\text{Ho}_2\text{Hf}_2\text{O}_7$ nanoparticles calcined at 700°C for (a) 2 h and (b) 6 h. Patterns are indexed by ICDD, 00-024-0473 indicating the miller indices of $\text{Ho}_2\text{Hf}_2\text{O}_7$ shown at the top of the peaks

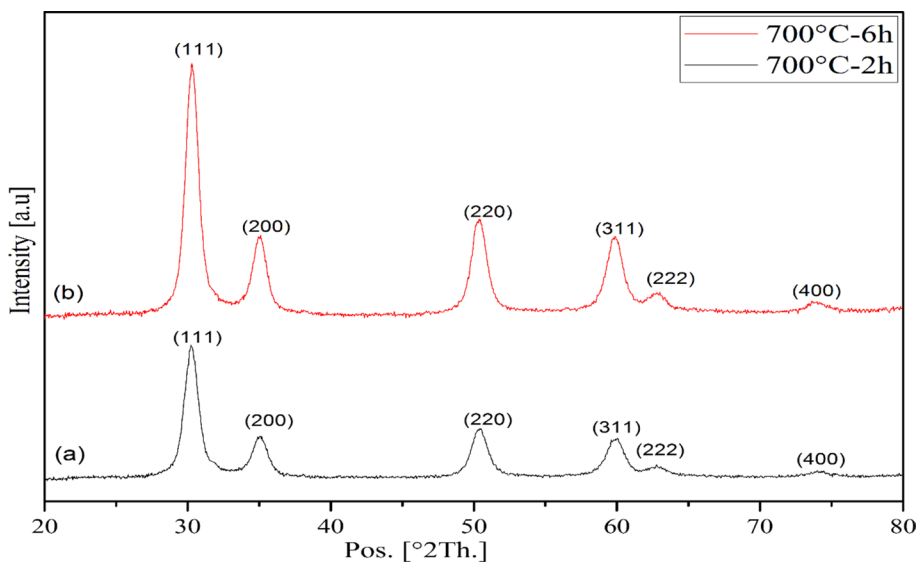
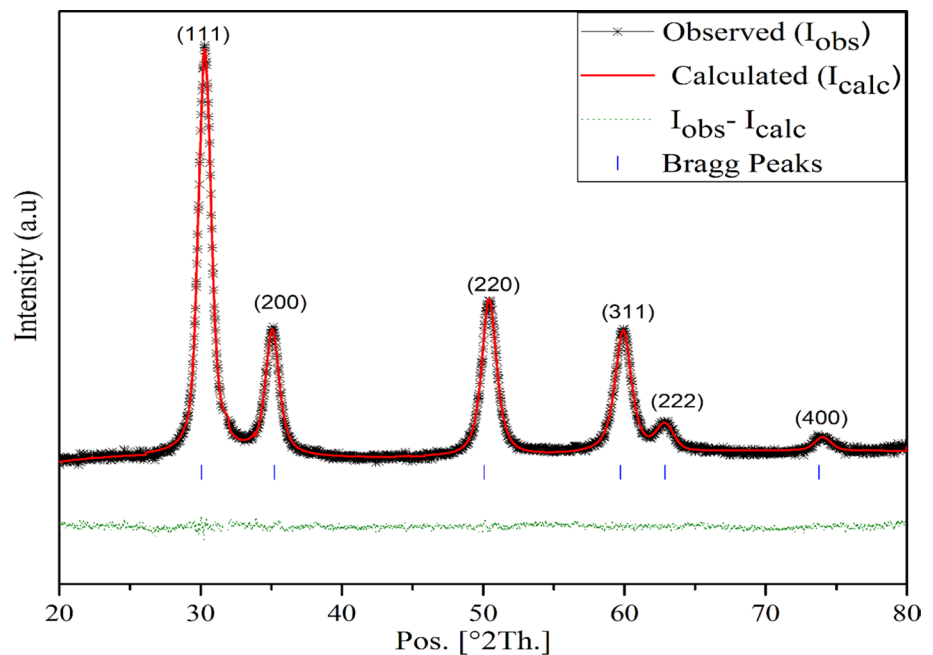


Table 1 Structural parameters of $\text{Ho}_2\text{Hf}_2\text{O}_7$

Sample heat treatment	Rietveld refined size strain analysis					
	Avg. crystallite size (nm)	Micro strain (%)	R_{wp} (%)	R_{exp} (%)	GOF	Lattice parameters (\AA)
700°C -2 h	5.40 (0.05)	2.237 (0.02)	3.4	3.27	1.04	5.1280
700°C -6 h	6.10 (0.08)	1.18 (0.015)	2.84	2.45	1.34	5.1308

Fig. 6 Rietveld refined ambient XRD patterns of $\text{Ho}_2\text{Hf}_2\text{O}_7$ nanoparticles calcined at 700 °C for 6 h with Miller indices representing fluorite structure



Crystallite size of sample was calculated applying the Scherrer's equation to the XRD pattern shown in Fig. 5. Crystallite size was obtained after eliminating instrument broadening and stress-strain broadening. The observed data and refined model are in good agreement as the sample shows approximately 3% weighted residual (Rwp) from refinement. Coarsening increased with increase in annealing time, and correspondingly the micro-strain decreased. With the rise in annealing time the particles aggregate and resultantly increase in particle size was observed. The lattice parameters of metallic nanoparticles contract with decrease in particle size in an inverse function of the diameters of nanoparticles [24].

The peaks were assigned with their Miller indices using reference pattern. Unit cell parameters of holmium hafnate lattice were modified during Rietveld refinement to best fit the experimental XRD pattern and compared well with reference pattern.

Stable defect fluorite structured nanopowder of $\text{Ho}_2\text{Hf}_2\text{O}_7$ with unit cell lattice parameters $a = b = c = 5.1308 \text{ \AA}$ and $\alpha = \beta = \gamma = 90^\circ$ were prepared employing LAP which is in excellent agreement with the corresponding values reported in literature of $\text{Ho}_2\text{Hf}_2\text{O}_7$ obtained mechanochemically [14, 15] and thermodynamically [16]. XRD reference pattern (ICDD-00-024-0473) considered as standard for the determination of the lattice parameters and a standard deviation (σ) of 0.0346 was found.

As XRD techniques are not sufficient to analyse the structural features of light atoms such as oxygen, Raman spectroscopy was used to support these inferences. Peaks identified in Raman spectra were fitted using suitable

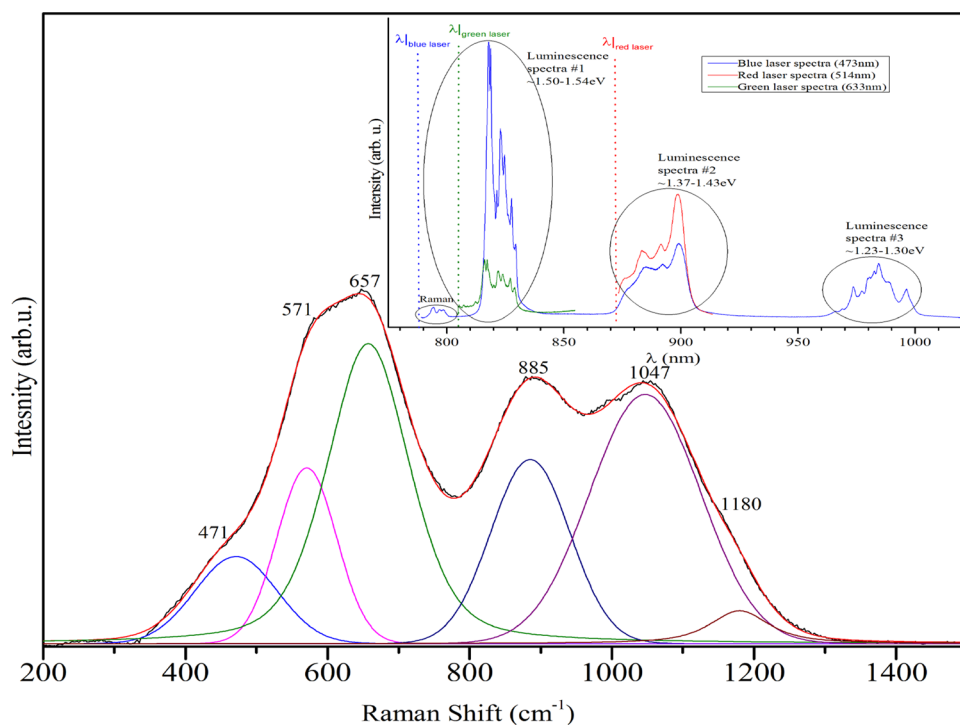
logarithmic functions to understand true Raman features. Raman peaks were fitted using Lorentz function which is suitable fitting technique for crystallised phases [25]. Lorentz function can be used to obtain wavenumber, area, height and FWHM (full width at half maximum) from a single Raman peak which provide distinct information about the material. Wavenumber (Raman shift) from Raman peak is distinctive to differentiate materials as each ionic group has unique wavenumber under laser excitation [26]. FWHM is relevant to the degree of crystallisation of materials [27]; increase in width suggests less crystallinity. Remaining two features are related to quantitative information of material; peak height and peak area [28]. Raman spectroscopy was employed to understand the material formed. Peaks in the Raman spectra were analysed using Origin Pro software.

Pyrochlore oxides have six theoretical Raman active modes [16, 29–37]

$$\Gamma_{\text{Raman}} = A_{1g} + E_g + 4F_{2g} \quad (1)$$

These Raman active modes represent the vibrations of $\langle \text{Ln-O} \rangle$ and $\langle \text{Hf-O} \rangle$ bonds [14, 32–40]. Raman spectroscopy is more suitable to study anion disorder in pyrochlores as these modes involve motion of oxygen atoms. Five modes ($A_{1g} + E_g + 3F_{2g}$) contribute to O_{48f} vibrations and O_{8b} vibrations yield a single F_{2g} mode [32, 41]. Raman spectra of $\text{Ho}_2\text{Hf}_2\text{O}_7$ nanopowder is shown in Fig. 7 acquired using 473 nm excitation wavelength. Raman modes observed at 571, 657, 885 cm^{-1} correspond to Ho–O stretch. Weak band around 1047 cm^{-1} resulted due to stretching of Hf–O. Spectra in Fig. 7 shows some initial

Fig. 7 Raman Spectra of $\text{Ho}_2\text{Hf}_2\text{O}_7$ nanopowder with excitation wavelength of 473 nm and fitted peaks. Inset shows the luminescence spectra with laser wavelengths of 473 nm, 514 nm and 633 nm



pyrochlore type short range ordering of cation and oxygen vacancies [27–29]. Broad band from 350 to 450 cm^{-1} can be associated to compositional substitution by atoms with mismatched atomic radii and valencies [42]. Here Raman spectra confirms the defect-fluorite structure of holmium hafnate as the band around $\sim 750 \text{ cm}^{-1}$ is breathing mode attributed to distortions in HfO_6 octahedra which strictly should not be present in perfect pyrochlore structure [29]. A band around 530 cm^{-1} can be explicitly assigned to the A_{1g} mode of pyrochlore phase [13, 43], which is also absent in Fig. 7.

Inset of Fig. 7 shows the photoluminescence (PL) spectra of $\text{Ho}_2\text{Hf}_2\text{O}_7$ with excitation wavelengths of 473 nm (blue), 514 nm (green) and 633 nm (Red). Raman spectra shown in Fig. 7 was observed below 800 nm. It is known that with the change in excitation wavelength the Raman bands shift the same amount correspondingly while the PL lines stay on the same wavenumber [40]. With 473 nm and 633 nm, $^5F_4/^5S_2 \rightarrow ^5I_7$ transition [44] bands were seen at around wavelength of 850–890 nm showing the PL nature of this band by staying on the same position. The corresponding excitation energy range with this band is ~ 1.37 to 1.43 eV. It is quite evident that under the excitation wavelength of 514 nm the PL lines from $^5F_4/^5S_2 \rightarrow ^5I_8$ transition [44] are so intense that they suppressed the traditional Raman spectra of holmium hafnate. Equivalent wavelength and excitation energy range with this band is 810–830 nm and ~ 1.50 to 1.54 eV respectively (Luminescence spectra #1 in Fig. 7). An important finding from the above

analysis is that Raman scattering and PL under 473 nm excitation wavelength can occur simultaneously as two separate optical processes for $\text{Ho}_2\text{Hf}_2\text{O}_7$ nanopowders. The selection of appropriate wavelength is an important factor for Raman study.

The morphology of obtained nanopowder of $\text{Ho}_2\text{Hf}_2\text{O}_7$ was investigated using Transmission Electron Microscope (FEI Tecnai TF20 FEG-TEM). Gatan Microscopy Suite (GMS) software was used for the analysis of TEM images and Selected Area Electron Diffraction (SAED) patterns. TEM images and SAED pattern of $\text{Ho}_2\text{Hf}_2\text{O}_7$ nanopowder calcined at 700 $^\circ\text{C}$ for 2 h are shown in Fig. 8. Inset shows the area enclosed with red circle for SAED pattern. Holmium hafnate nanoparticles are of uniform shape with narrow size distribution and crystalline in nature (Table 3). Results from TEM confirmed the XRD analysis. XRD peak broadening and less sharp SAED rings indicate smaller crystallite size for annealing time of 2 h.

TEM images of holmium hafnate nanoparticles calcined at 700 $^\circ\text{C}$ for 6 h are shown in Fig. 9. Inset shows the area encircled red for SAED pattern. SAED rings and XRD patterns were compared and all the values of Miller indices (hkl) are in good agreement with XRD reference pattern (ICDD, 00-024-0473). Table 2 shows the d-spacing calculated from TEM and XRD data for different crystal planes. Interplanar spacing (d-spacing) agreed well in case of XRD, TEM (SAED) and reference pattern (Table 2).

More spots appearing in the ring pattern in Fig. 9 compared with Fig. 8 indicate the relatively larger crystallite size of $\text{Ho}_2\text{Hf}_2\text{O}_7$ nanoparticles of sample calcined

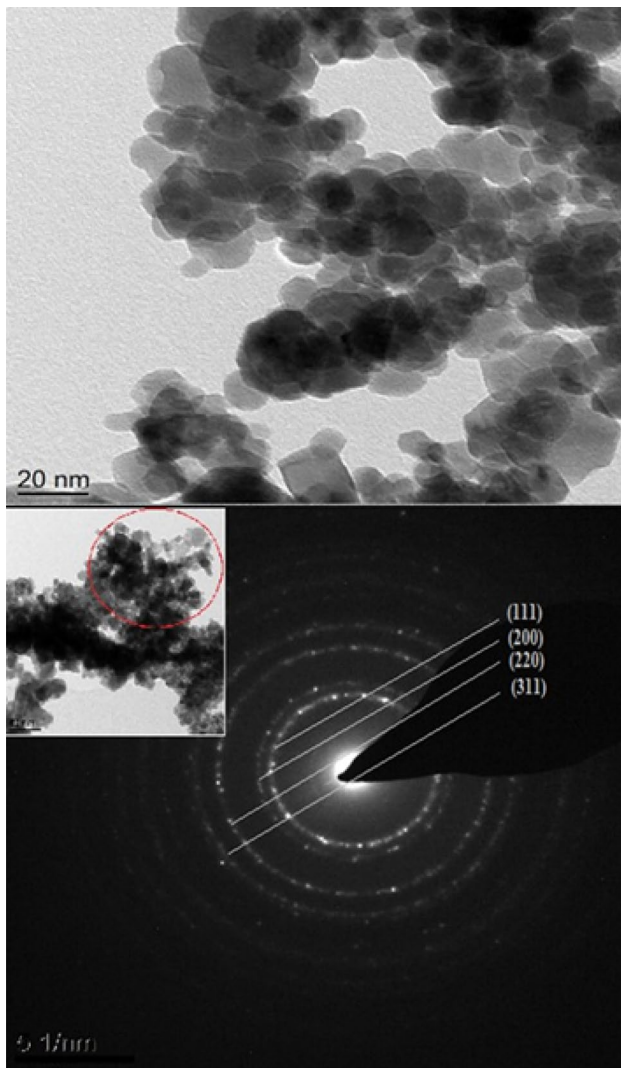


Fig. 8 TEM images with SAED pattern of $\text{Ho}_2\text{Hf}_2\text{O}_7$ calcined at $700\text{ }^\circ\text{C}$ for 2 h

for 6 h at $700\text{ }^\circ\text{C}$. This is in agreement with the results of XRD and TEM analysis shown in Table 1 and 2.

Grain sizes from Figs. 8 and 9 were calculated using ImageJ and are shown in Table 3. Holmium hafnate nanoparticles show narrow size distribution and with the increase in calcination duration grain size increases.

Energy Dispersive X-ray (EDX) spectroscopy was used to study the composition of holmium hafnate nanoparticles. Figure 10 shows the EDX analysis of Fig. 9 and it confirms the presence of Ho, Hf and O in the same ratio as in the stoichiometry of the material. Peaks due to C and Cu are attributed to the holey carbon copper mesh grid used for TEM–EDX analysis. The inset in Fig. 10 shows the atomic percent of elements obtained from EDX analysis which agrees very well with the theoretical values of 18.2 at% for Ho, 18.2 at% for Hf and 63.6 at%

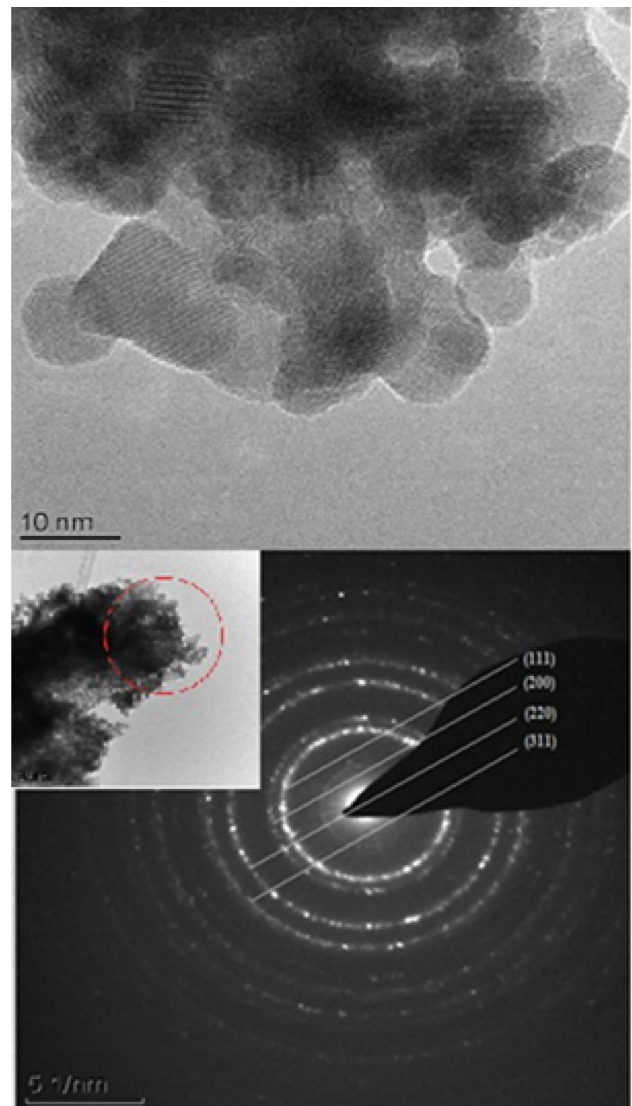


Fig. 9 TEM images with SAED pattern of $\text{Ho}_2\text{Hf}_2\text{O}_7$ calcined at $700\text{ }^\circ\text{C}$ for 6 h

for O indicating that the compound exhibit negligible non-stoichiometry.

A HR-TEM image of $\text{Ho}_2\text{Hf}_2\text{O}_7$ nanopowder calcined at $700\text{ }^\circ\text{C}$ for 6 h is shown in Fig. 11. Lattice planes can be easily seen and indexed as (311). Nanoparticles of $\text{Ho}_2\text{Hf}_2\text{O}_7$ showed the crystalline phase formation with cubic structure and interplanar distance of 1.51 \AA which correspond to the (311) plane. HR-TEM image of holmium hafnate powder prepared by solid state reaction through mechanical milling was reported in literature [15]. The interplanar distance calculated by Shojan et al. [15] is 2.60 \AA for (X00) plane is in good agreement for (200) plane as shown in Table 2. Using high purity feed material nanoparticles of $\text{Ho}_2\text{Hf}_2\text{O}_7$ can be successfully prepared by employing novel Leeds Alginate Process (LAP) at significantly low

Table 2 Comparison of d-spacing of holmium hafnate from TEM and XRD rietveld refinement

h	k	l	Ref. (ICDD-00-024-0473) d (Å)	XRD d (Å)		TEM d (Å)	
				700 °C-2 h	700 °C-6 h	700 °C-2 h	700 °C-6 h
1	1	1	3.00600	2.95158	2.95049	3.00	2.94
2	0	0	2.60400	2.55749	2.55665	2.54	2.52
2	2	0	1.84100	1.81032	1.80979	1.79	1.78
3	1	1	1.57000	1.54445	1.54402	1.53	1.51

Table 3 Grain size analysis of holmium hafnate nanopowders from TEM images

	Size range (nm)	Avg. grain size (nm)
700 °C-2 h	8.5–12.5	10.3
700 °C-6 h	14–18	17.36

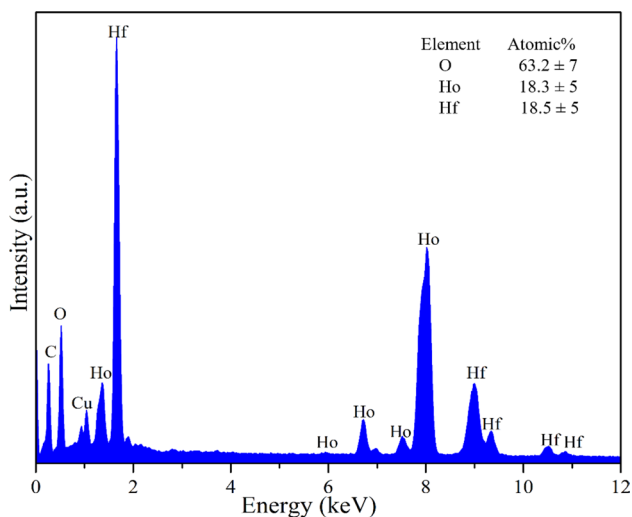


Fig. 10 EDX analysis of Ho₂Hf₂O₇ nanopowders calcined at 700 °C for 6 h

temperature (~ 600 °C) and in an energy efficient manner compared with other processes [14–16].

Nanopowders of holmium hafnate were pressed into pellet and sintered at 1500 °C for 2 h. Ac-impedance spectroscopy was carried out at selected three temperatures i.e. 400 °C, 600 °C and 750 °C between 100 mHz and 100 MHz on the obtained ceramic sample of holmium hafnate and the preliminary data of bulk and grain boundary conductivity of Ho₂Hf₂O₇ is reported in the Table 4. There has been no sign of grain boundary contribution to the total conductivity of Ho₂Hf₂O₇ at 400 °C and the ionic conductivity is solely due to the bulk oxide-ion migration however with the increase in temperature bulk and grain boundary contribution

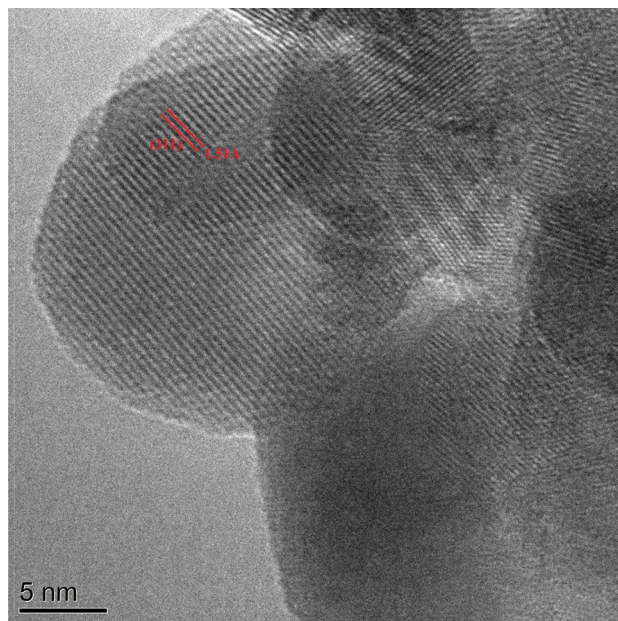


Fig.11 HR-TEM image of Ho₂Hf₂O₇ powder with defect-fluorite structure and interplanar spacing of 1.51 Å along the (311) direction

Table 4 Bulk and grain boundary conductivity of Ho₂Hf₂O₇ pellet

Temperature (°C)	Bulk conductivity (S cm ⁻¹)	Grain boundary conductivity (S cm ⁻¹)
400	1.44 × 10 ⁻⁷	
600	1.15 × 10 ⁻⁵	6.35 × 10 ⁻⁶
750	2.44 × 10 ⁻⁴	1.22 × 10 ⁻⁴

were distinctly observed. The values of the activation energies were 1.24 (± 0.01) eV for bulk conductivity and 1.55 (± 0.01) eV for grain boundary conductivity. Details on the ionic conductivity of similar material Ho₂Zr₂O₇ synthesised employing LAP has been recently reported by Sardar et al. [45] which further supports that Ho₂Hf₂O₇ is a promising material for SOFC electrolyte.

4 Conclusions

Nanoparticles of holmium hafnate were successfully synthesised using the Leeds Alginate Process (LAP). Thermal analysis of prepared metal alginate beads using TGA/DSC is in confirmation with the HT-XRD data as onset and endset of decomposition is similar in both cases. Following these conclusions calcination temperature of 700 °C was determined. XRD analysis exhibits that single phase cubic nanoparticles of $\text{Ho}_2\text{Hf}_2\text{O}_7$ with defect-fluorite structure and space group of $Fm\bar{3}m$ were obtained. Analysis from Raman spectra confirms the defect-fluorite structure of $\text{Ho}_2\text{Hf}_2\text{O}_7$. Raman scattering and photoluminescence under 473 nm excitation wavelength can occur simultaneously as two separate optical processes for $\text{Ho}_2\text{Hf}_2\text{O}_7$ nanopowders. Values of interplanar spacing obtained from characterization techniques of XRD and TEM agree with each other as well as XRD reference pattern. Crystallite size is affected by the calcination duration. With the increase in calcination duration from 2 to 6 h crystallite size increased from 5.40 to 6.10 nm. TEM analysis is carried out and peaks from XRD data and lattice planes from SAED rings are in good agreement. The d-spacing values obtained from Rietveld refinement and SAED are comparable as well. Grain size analysis from TEM images confirms the narrow size distribution and increase in grain size with increase in calcination duration. TEM-EDX analysis confirm that $\text{Ho}_2\text{Hf}_2\text{O}_7$ is stoichiometric. Raman spectroscopy shows the evidence of oxide-ion vacancy which is further confirmed by the temperature dependence of the ac-impedance measurement of $\text{Ho}_2\text{Hf}_2\text{O}_7$. The LAP has capability to successfully yield pyrochlore oxide nanoparticles of electrolyte materials for solid oxide fuel cells. Pyrochlore oxides with defect fluorite structure are known to be good oxide ion conductors and potential materials as solid oxide fuel cell (SOFC) electrolytes.

Acknowledgements Financial support for the first author from the Commonwealth Scholarship Commission (CSC), UK (PKCA-2016-93) is gratefully acknowledged.

Compliance with ethical standards

Conflict of interest The authors declare no competing financial interests.

Open Access This article is licensed under a Creative Commons Attribution 4.0 International License, which permits use, sharing, adaptation, distribution and reproduction in any medium or format, as long as you give appropriate credit to the original author(s) and the source, provide a link to the Creative Commons licence, and indicate if changes were made. The images or other third party material in this article are included in the article's Creative Commons licence, unless indicated otherwise in a credit line to the material. If material is not

included in the article's Creative Commons licence and your intended use is not permitted by statutory regulation or exceeds the permitted use, you will need to obtain permission directly from the copyright holder. To view a copy of this licence, visit <http://creativecommons.org/licenses/by/4.0/>.

References

1. Yang L, Wang SZ, Blinn K, Liu MF, Liu Z, Cheng Z, Liu ML (2009) Enhanced sulfur and coking tolerance of a mixed ion conductor for SOFCs: $\text{BaZr}_{0.1}\text{Ce}_0.9\text{Y}_{0.2-x}\text{Yb}_x\text{O}_{3-d}$. *Science* 326:126–129
2. Yong-II Kim MKJ, Won-Bin I (2013) Crystal structural study of Ho-doped ceria using X-ray powder diffraction data. *J Electroceram* 31:254–259
3. Kilner JA, Burriel M (2014) Materials for intermediate-temperature solid-oxide fuel cells. *Annu Rev Mater Res* 44:365–393
4. Nakajo A (2007) Enhancement of lifetime of SOFC stacks for combined heat and power application. Final Report, EPFL-LENI
5. Wuensch BJ, Eberman KW, Heremans C, Ku EM, Onnerud P, Yeo EME, Haile SM, Stalick JK, Jorgensen JD (2000) Connection between oxygen-ion conductivity of pyrochlore fuel-cell materials and structural change with composition and temperature. *Solid State Ion* 129:111–133
6. Diaz-Guillen JA, Fuentes AF, Diaz-Guillen MR, Almanza JM, Santamaria J, Leon CJ (2009) The effect of homovalent A-site substitutions on the ionic conductivity of pyrochlore-type $\text{Gd}_2\text{Zr}_2\text{O}_7$. *J Power Sources* 186:349–352
7. Jones RL (1997) Some aspects of the hot corrosion of thermal barrier coatings. *J Therm Spray Technol* 6:77–84
8. Jones R, Williams C (1987) Hot corrosion of CoCrAlY by molten sulfate-vanadate deposits. *Mater Sci Eng* 87:353–360
9. Deepa M, Prabhakar RP, Radhakrishnan AN, Sibi KS, Koshy P (2009) Pyrochlore type semiconducting ceramic oxides in Ca–Ce–Ti–M–O system (M = Nb or Ta)—structure, microstructure and electrical properties. *Mater Res Bull* 44:1481–1488
10. Blanchard PER, Liu S, Kennedy BJ, Ling CD (2013) Investigating the local structure of lanthanoid hafnates $\text{Ln}_2\text{Hf}_2\text{O}_7$ via diffraction and spectroscopy. *J Phys Chem C* 117:2266–2273
11. Zhou LX, Fisher D, Templeton J (2010) High-performance ultrathin film solid oxide fuel cell using anodized-aluminium-oxide supporting structure. *Electrochem Commun* 2(2):179–182
12. Wang Z, Kale GM, Ghadiri M (2012) Synthesis and characterization of $\text{Ce}_x\text{Gd}_{1-x}\text{O}_{2-d}$ nanopowders employing an alginate mediated ion-exchange process. *Chem Eng J* 198:149–153
13. Wang Z, Kale GM, Ghadiri M (2012) Novel ion-exchange process for the preparation of metal oxide nanopowders from sodium alginate. *J Am Ceram Soc* 95:3124–3129
14. Lopez-Cota FA, Cepeda-Sanchez NM, Diaz-Guillen JA, Dura OJ, Lopez OMA, Maczka M, Ptak M, Fuentes AF (2017) Electrical and thermophysical properties of mechanochemically obtained lanthanide hafnates. *J Am Ceram Soc* 100:1994–2004
15. Shojan P, Pavunni YS, Sudheendran K, Sita D, Rajesh KK, James FS, Ram SK (2015) Holmium hafnate: an emerging electronic device material. *Appl Phys Lett* 106:112902
16. Mandal BP, Garg N, Sharma SM, Tyagi AK (2006) Preparation, XRD, and Raman spectroscopic studies on new compounds $\text{RE}_2\text{Hf}_2\text{O}_7$ (RE = Dy, Ho, Er, Tm, Lu, Y): pyrochlores or defect-fluorite? *J Solid State Chem* 179:1990–1994
17. Gombotz WR, Wee SF (1998) Protein release from alginate matrices. *Adv Drug Deliv Rev* 31(3):267–285

18. Wang Z, Kale GM, Yuanb Q, Ghadiri M (2012) X-Ray microtomography of freeze dried nickel alginate beads and transformation into NiO nanopowders. *RSC Adv* 2:9993–9997
19. Wang Z, Comyn TP, Ghadiri M, Kale GM (2011) Maltose and pectin assisted sol–gel production of $\text{Ce}_{0.8}\text{Gd}_{0.2}\text{O}_{1.9}$ solid electrolyte nanopowders for solid oxide fuel cells. *J Mater Chem* 21(41):16494–9
20. Rahayu S, Forrester JS, Kale GM, Ghadiri M (2018) Promising solid electrolyte material for an IT-SOFC: crystal structure of the cerium gadolinium holmium oxide $\text{Ce}_{0.8}\text{Gd}_{0.1}\text{Ho}_{0.1}\text{O}_{1.9}$ between 295 and 1023 K. *Acta Cryst C* 74:236–239
21. Rietveld HM (1969) A profile refinement method for nuclear and magnetic structures. *J Appl Crystallogr* 2:65–71
22. Young RA (1993) The rietveld method. Oxford University Press Inc, New York
23. Gladman T (2004) Grain size control. Maney Publishing, Leeds
24. Vermaak JS, Mays CW, Kuhlmann-Wilsdorf D (1968) On surface stress and surface tension: I. Theoretical considerations. *Surf Sci* 12:128
25. Liao TW, Chen HM, Shen KY, Kuan CH (2015) Pure, single crystal Ge nanodots formed using a sandwich structure via pulsed UV excimer laser annealing. *Nanotechnology* 26(16):65301
26. Long DA (1997) Raman spectroscopy. McGraw-Hill International Book Company, New York
27. Tsao CY, Weber JW, Campbell P, Widenborg PI, Song D, Green MA (2009) Low temperature growth of polycrystalline Ge thin film on glass by in situ deposition and ex situ solid-phase crystallization for photovoltaic applications. *Appl Surf Sci* 255(15):7028–7035
28. Katainen E, Elomaa M, Laakkonen UM, Sippola E, Niemela P, Suhonen J, Jarvinen K (2007) Quantification of the amphetamine content in seized street samples by Raman spectroscopy. *J Forensic Sci* 52(1):88–92
29. Blanchard PER, Liu S, Kennedy BJ, Ling CD, Avdeev M, Aitken JB, Cowie BCC, Tadich A (2013) Investigating the local structure of lanthanoid hafnates $\text{Ln}_2\text{Hf}_2\text{O}_7$ via diffraction and spectroscopy. *J Phys Chem* 115:2266–2273
30. Gupta HC, Brown S, Rani N, Gohel VB (2002) A lattice dynamical investigation of the Raman and the infrared frequencies of the cubic $\text{A}_2\text{Hf}_2\text{O}_7$ pyrochlores. *J Phys Chem Solids* 63:535–538
31. Kumar S, Gupta HC (2012) First principles study of dielectric and vibrational properties of pyrochlore hafnates. *Solid State Sci* 14:1405–1411
32. Vandendorre MT, Husson E (1983) Comparison of the force field in various pyrochlore families. I. The $\text{A}_2\text{B}_2\text{O}_7$ Oxides. *J Solid State Chem* 50:362–371
33. Vandendorre MT, Husson E (1984) Comparison of the force field in various pyrochlore families II. Phases presenting structural defects. *J Solid State Chem* 53:253–259
34. Vandendorre MT, Husson E, Chattry JP, Michel D (1983) Rare-earth titanates and stannates of pyrochlore structure; vibrational spectra and force fields. *J Raman Spectrosc* 14:63–71
35. Scheetz BE, White WB (1983) Temperature-dependent Raman spectra of rare-earth titanates with the pyrochlore structure: a dipolar order-disorder transition. *Opt Eng* 22:223302
36. Poulsen FW, Glerup M, Holtappels P (2000) Structure, Raman spectra and defect chemistry modelling of conductive pyrochlore oxides. *Solid State Ion* 135:595–602
37. Saha S et al (2006) High-pressure Raman and X-ray study of the spin-frustrated pyrochlore $\text{Gd}_2\text{Ti}_2\text{O}_7$. *Phys Rev B* 74:064109
38. Lian J, Zu XT, Kuttly KVG, Chen J, Wang LM, Ewing RC (2000) Ion-irradiation-induced amorphization of $\text{La}_2\text{Zr}_2\text{O}_7$ pyrochlore. *Phys Rev B* 66:054108
39. Solomon JM, Shamblin J, Lang M, Navrotsky A, Asta M (2016) Chemical ordering in substituted fluorite oxides: a computational investigation of $\text{Ho}_2\text{Zr}_2\text{O}_7$ and $\text{Re}_2\text{Th}_2\text{O}_7$ (RE = Ho, Y, Gd, Nd, La). *Sci Rep* 6:1–9
40. Stanek CR, Grimes RW (2002) Prediction of rare earth $\text{A}_2\text{Hf}_2\text{O}_7$ pyrochlore phases. *J Am Ceram Soc* 86:2139–2141
41. Maczka M, Sanjuan ML, Fuentes AF, Hermanowicz K, Hanuza J (2008) Temperature-dependent Raman study of the spin-liquid pyrochlore $\text{Tb}_2\text{Ti}_2\text{O}_7$. *Phys Rev B* 78(8):134420
42. Hess NJ, Begg BD, Conradson SD, Mccready DE, Gassman PL, Weber WJ (2002) Radiation-induced disorder in compressed lanthanide zirconates. *J Phys Chem B* 106:4663
43. Maczka M, Sanjuan ML, Fuentes AF et al (2009) Temperature-dependent studies of the geometrically-frustrated pyrochlores $\text{Ho}_2\text{Ti}_2\text{O}_7$ and $\text{Dy}_2\text{Ti}_2\text{O}_7$. *Phys Rev B* 79(13):214437
44. Lu DY, Guan DX (2017) Photoluminescence associated with the site occupations of Ho^{3+} ions in BaTiO_3 . *Sci Rep* 7:6125
45. Sardar S, Kale GM, Ghadiri M (2020) Influence of processing conditions on the ionic conductivity of holmium zirconate ($\text{Ho}_2\text{Zr}_2\text{O}_7$). *Ceram Int*. <https://doi.org/10.1016/j.ceramint.2020.01.177>

Publisher's Note Springer Nature remains neutral with regard to jurisdictional claims in published maps and institutional affiliations.